

pubs.acs.org/JPCC Article

Tuning the Band Gaps of Oxide and Halide Perovskite Compounds via Biaxial Strain in All Directions

Corey Teply, Britt A. Tyler, and Robert F. Berger*



Cite This: J. Phys. Chem. C 2021, 125, 25951-25958



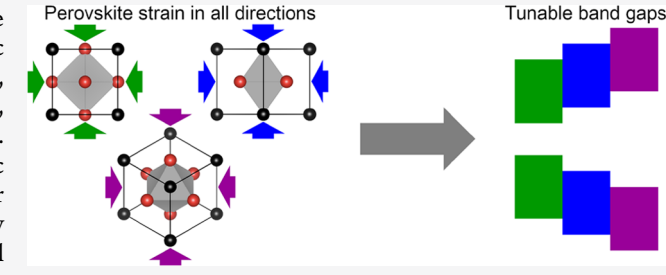
ACCESS

Metrics & More

Article Recommendations

Supporting Information

ABSTRACT: Perovskite compounds in the oxide and halide families have generated interest as light absorbers for photocatalytic and photovoltaic applications, respectively. In both of these classes, biaxial strain can be used to tune structural distortions and, consequently, band gaps and solar energy conversion efficiencies. While strain has usually been explored perpendicular to the cubic perovskite unit cell axis (i.e., the 001 direction), strain in other crystallographic directions presents opportunities for qualitatively different changes to the electronic structure or even a range of local band gaps within the same material. For oxide (BaTiO₃) and halide



(CsGeX₃) perovskites with polar ferroelectric distortions at room temperature, the present work explores how and why strain in all crystallographic directions tunes the band gap and band-edge orbitals. It is determined that, for reasons traceable to the interactions of atomic orbitals at the band edges, the band gaps of both oxide and halide compounds under achievable compressive biaxial strains vary by several tenths of an eV depending on the direction of strain. Notably, the range of band gaps accessible in CsGeI₃ is predicted to span the most intense regions of the solar spectrum.

■ INTRODUCTION

Perovskite compounds (ABX₃) have shown promise as lightabsorbing materials for solar energy conversion. Oxide perovskites (e.g., SrTiO₃) have been studied as solar photocatalysts for reactions such as water splitting for several decades.^{1–5} Halide perovskites (e.g., CH₃NH₃PbI₃) have more recently become the subject of extremely active study in photovoltaics.^{6–9} Because the composition and atomic structure of perovskites can be modified in a variety of ways (e.g., doping and substitution,^{10–17} defects,^{18–21} and reduced dimensionality^{22–26}), there are ongoing experimental and computational efforts to tune their band structures, band gaps, and optoelectronic properties.

Among these modes of perovskite tunability is biaxial strain. In the most controlled manifestation of biaxial strain, epitaxial thin films can be grown on perovskite substrates varying in unit cell size, such that the in-plane axes of the perovskite film are compressed or stretched by up to approximately ±3%. This type of synthesis has been done extensively for oxide perovskites^{27–29} and has been developed more recently for halides.^{30–33} While such films have most often been grown in the 001 direction resulting in films strained perpendicular to the 001 axis (i.e., a B–X bond axis), they can in principle be grown on different substrate surfaces to achieve strain perpendicular to other axes. Even apart from epitaxial thin films, perovskite materials and nanostructures with defects often have nonuniform, local internal strains. Therefore, a perovskite material may be subjected to biaxial strains in a

variety of directions, sometimes multiple directions, within a given sample.

The possibility of strain in a variety of crystallographic directions presents complex fundamental questions of how the direction of strain can be used to tune structural distortions in perovskite compounds and consequently, their electronic structure and band gap. It also hints at opportunities for technological applications, as a material with a variety of nonuniform internal strains could have a range of band gaps—and could therefore absorb light in different parts of the solar spectrum and harness a larger fraction of solar energy, akin to a multijunction solar cell.

In this paper, we explore the relationships among the magnitude and direction of perovskite strain, the resulting structural distortions, and features of the band-edge orbitals and band gaps. Compounds with polar ferroelectric distortions at room temperature—an oxide (BaTiO₃) and a family of halides (CsGeX₃)—are the main focus of this work because such distortions allow for significant tunability as a function of the direction of strain. Ferroelectric materials have generated significant interest in solar energy conversion.^{34–36} While

Received: August 12, 2021 Revised: October 29, 2021 Published: November 21, 2021





germanium-halide perovskites are challenging to synthesize as films and tend to oxidize from Ge2+ to Ge4+, CsGeI3 and other AGeI₃ compounds have been identified as promising materials for photovoltaic applications due to their appropriate band gaps and band offsets, 37,38 favorable electronic structure for hole transport,³⁹ and (relevant to this work) tunability under hydrostatic pressure. 40 Given the current interest in lead-halide perovskite solar cells, we also briefly discuss the case of CsPbI₃ (a compound with octahedral rotations rather than ferroelectric distortion). We focus on trends in band gap and bandedge orbitals, highlighting similarities and differences between the oxide and halide families. The results presented in this paper enable quantitative predictions of band gap tunability with an eye toward solar energy conversion applications and fundamentally rationalize them based on qualitative features and trends in the near-gap band structure and orbital character.

■ COMPUTATIONAL METHODS

Crystal structures are optimized and band gaps are computed within density functional theory (DFT) using the VASP package $^{41-44}$ and PAW potentials. 45 A Γ -centered $6\times 6\times 6$ k-point mesh is used for unit cells with a single perovskite formula unit, while proportionally fewer k-points are used for structures with larger unit cells. When multiple options are available, pseudopotentials are chosen such that as many electrons are possible are computed explicitly (details in the Supporting Information 46). In cases where absolute band-edge energies are discussed, they are referenced to the energy of the flat, lowest-energy, semi-core band at k-point Γ (Ti 3s in BaTiO3, Ge 3d in CsGeX3, Cs 5s in CsPbI3).

Structural geometry optimizations employ the PBE functional 47 (a generalized gradient approximation) and a planewave basis set cutoff of 500 eV. Because PBE calculations tend to underestimate band gaps relative to experiments, a hybrid functional is used to compute most band gaps (with the exception of those of larger-unit-celled CsPbI₃). The HSE06 functional 48 is chosen for its ability to replicate the experimental band gaps of the relaxed room-temperature structures of BaTiO₃ (HSE06 = 3.23 eV, experiment = 3.2 eV 49) and CsGeI₃ (HSE06 = 1.53 eV, experiment = 1.63 eV 37). The basis set cutoff for these hybrid DFT calculations is 500 eV for BaTiO₃ and 350 eV for CsGeX₃.

Biaxial strain is modeled by fixing two Cartesian coordinates of each unit cell vector and allowing the third to relax. The magnitude of strain is expressed as a percent change in length relative to the optimized cubic unit cell size. For example, -2%strain refers to a case in which in-plane axis lengths are compressed by 2% relative to the optimized cubic cell. Most previous computational work has focused on strain perpendicular to the 001 axis (Figure 1a, left), modeling epitaxial thin films grown in the 001 direction. In this work, we focus on biaxial strain in all crystallographic directions, modeling thin films grown on a variety of surfaces, or more generally, the nonuniform internal strains present in real materials. Compressive strains perpendicular to high-symmetry axes (001, 011, and 111) are illustrated in Figure 1a. Given the cubic symmetry of the prototypical perovskite structure, a triangle connecting those three high-symmetry directions includes all unique directions of strain (Figure 1b). In this paper, perovskite compounds are computed with strains perpendicular to the 15 directions illustrated on the grid in Figure 1c. To ensure that the global energy minimum is identified for each direction of strain, the lowest-energy

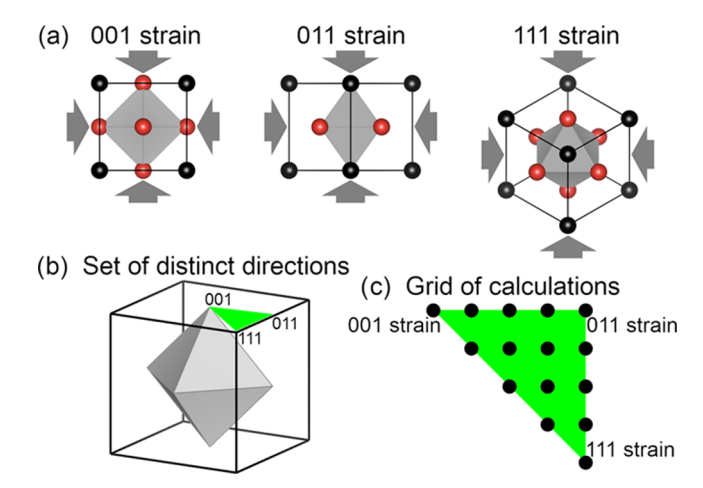


Figure 1. (a) High-symmetry directions of biaxial strain (001, 011, and 111) of a perovskite unit cell. (b) All unique directions are spanned by a triangle connecting these three high-symmetry directions. (c) A grid of 15 strain directions sampling this triangle is computed.

optimized structure is chosen from several calculations, with distortions initially oriented in a variety of directions.

It is worth noting that the DFT-computed structural geometries in this work are implicitly at zero temperature and lack the entropic contributions that may lead perovskite compounds to adopt higher-symmetry phases at higher temperatures. Still, there is reason to believe these computed zero-temperature geometries are strongly representative of what would be seen at higher temperatures. In BaTiO₃₁, for example, it has been shown through the agreement of experiment⁵⁰ and computation⁵¹ that the effect biaxial strain has on stabilizing and enhancing particular distortive modes at low temperature also expands the temperature range in which those distortions are observed. Therefore, while zero-temperature DFT calculations may not capture the details of the temperature dependence of phase transitions, they do capture changes in the preferred direction of distortion that accompany changes in the direction of strain.

■ RESULTS AND DISCUSSION

Effect of Strain on the Direction of Distortion. The room-temperature crystal structures of BaTiO₃ and CsGeI₃ are shown in Figure 2. Both feature ferroelectric distortion, in which their cation and anion sublattices are shifted slightly relative to each other. The presence of ferroelectric distortion in these compounds is often rationalized based on the relative sizes of their ions, invoking Goldschmidt tolerance factors⁵² or

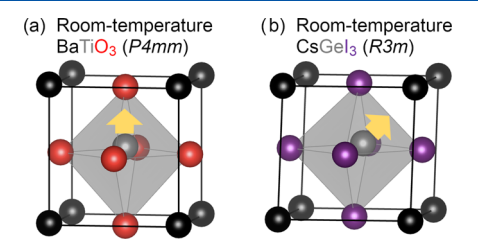


Figure 2. Room-temperature phases of (a) BaTiO₃ and (b) CsGeI₃. The former has polar ferroelectric distortion along the 001 axis, the latter along the 111 axis. Images of crystal structures throughout this paper are made using the software VESTA. 57

related ideas.⁵³ Because BaTiO₃ and CsGeI₃ have relatively large A-site cations and small B-site cations (resulting in respective tolerance factors of $t = \frac{r_A + r_X}{\sqrt{2} \left(r_B + r_X \right)} = 1.06$ and 0.98 based on their Shannon crystal radii⁵⁴), both see their B-site cations shift within their octahedral cages. In room-temperature BaTiO₃ (Figure 2a), the distortion is oriented in the 001 direction, resulting in tetragonal *P4mm* space group symmetry.⁵⁵ In room-temperature CsGeI₃ and the corresponding bromide and chloride compounds (Figure 2b), the distortion is oriented in the 111 direction, resulting in rhombohedral *R3m* space group symmetry.⁵⁶

When biaxial strain is applied to these compounds, the direction of ferroelectric distortion may be altered. In general, ions tend to shift in such a way that they maintain physically reasonable distances from their nearest neighbors. For example, when in-plane compressive strain threatens to shorten the distance between a B-site cation and its X-site neighbors, the B-site cation tends to shift in the perpendicular direction to avoid these close contacts. Therefore, compressive strain is expected to lead to ferroelectric distortion along or near the axis perpendicular to the strain. Somewhat less consistently, tensile strain is expected to lead to ferroelectric distortion close to the plane of strain.

These expectations are borne out in Figure 3. As a function of the direction of biaxial strain, the plots show the direction in

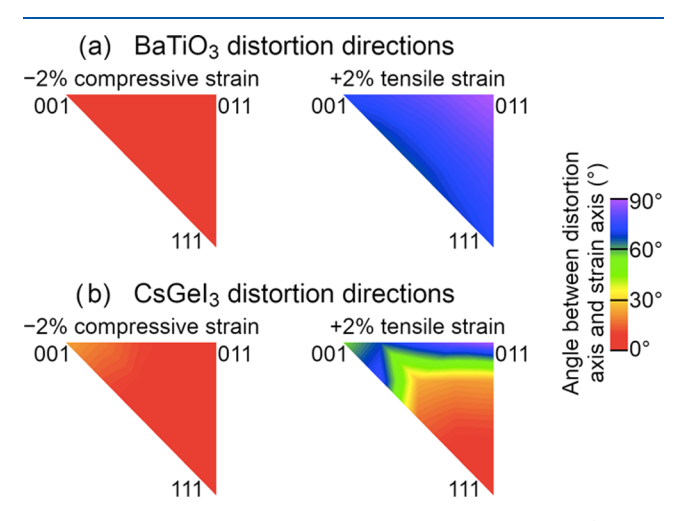


Figure 3. Plots of the orientation of ferroelectric distortion (i.e., the direction in which the B-site cation shifts among its nearest neighbors) in (a) BaTiO $_3$ and (b) CsGeI $_3$ under biaxial strain in various directions. Plots on the left show -2% (compressive) strain, while plots on the right show +2% (tensile) strain. Angles are defined such that 0° points along the axis perpendicular to the strain, while 90° points in the plane of strain.

which the B-site cation shifts away from the center of its octahedron of nearest neighbors, expressed as an angle from the axis perpendicular to the strain. To clarify, 0° refers to distortion along the axis perpendicular to the strain, while 90° refers to distortion in a direction in the plane of strain. For BaTiO₃ under -2% compressive strain (Figure 3a, left), all directions of strain result in distortions at angles less than 7°. This suggests that it is possible to induce a distortion along a desired axis of BaTiO₃ by applying compressive strain perpendicular to that axis. The results are similar for CsGeI₃ under -2% compressive strain (Figure 3b, left), in which all distortion angles are less than 24°. Distortions in CsGeI₃ are

less aligned with the axis perpendicular to the strain because of the strong natural tendency of CsGeI₃ to distort in the 111 direction in the absence of strain. In BaTiO₃ under +2% tensile strain (Figure 3a, right), distortion angles are all greater than 65°, relatively close to the plane of strain. In CsGeI₃ under +2% tensile strain (Figure 3b, right), distortion angles are less predictable, highly dependent on the direction of strain. The numerical results corresponding to Figure 3, as well as the qualitatively similar results for CsGeBr₃ and CsGeCl₃, are provided in the Supporting Information.

The ability to use strain to control the direction of ferroelectric distortion implies the ability to tune the electronic structure and band gap. This will be explored later in the paper after a brief overview of the band structure and band-edge orbitals of these classes of perovskites.

Near-Gap Electronic Structure of Oxide and Halide Perovskites. The basic features of the band structures and band-edge orbitals of oxide and halide perovskites have been described at length in previous work. ^{58–64} We briefly review some key points in this subsection in preparation to explore the optoelectronic effects of strain in all directions.

In d^0 transition metal oxides (BaTiO₃ and related compounds), the valence band consists primarily of filled oxide 2p states. Therefore, the valence band maximum (VBM) is the most antibonding combination of these states. In the undistorted cubic phase, the VBM lies at k-point R = (1/2, 1/2, 1/2), with threefold degenerate crystal orbitals residing in the xy-, xz-, and yz-planes. The conduction band consists primarily of unfilled B-site d states, of which the conduction band minimum (CBM) is the least antibonding combination. In the undistorted cubic phase, the CBM lies at k-point $\Gamma = (0, 0, 0)$ and consists of threefold degenerate nonbonding combinations of B-site t_{2g} states (d_{xy} , d_{xz} , and d_{yz}). The neargap band structure and computed electron densities of the band-edge crystal orbitals of cubic BaTiO₃ are shown in Figure 4a.

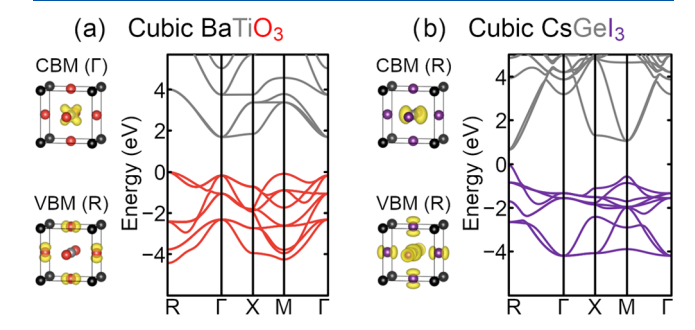


Figure 4. Near-gap DFT-PBE band structures and electron densities of the band-edge crystal orbitals for cubic (a) $BaTiO_3$ and (b) $CsGeI_3$. Isosurfaces of the electron densities associated with the band-edge crystal orbitals are shown in yellow. Valence bands are shown in color (red or purple), conduction bands in gray. The valence band maximum (VBM) is defined as zero energy.

In general, structural distortions in d^0 oxide perovskites are known to break the band-edge degeneracies in Figure 4a, shifting the energies of band-edge orbitals. Recent work in our group has shown that the crystallographic orientation of ferroelectric distortion in d^0 oxide perovskites has a significant impact on band gap, which can be rationalized based on crystal orbital symmetry and mixing. Specifically, distortion along a B–X bond axis (i.e., the 001 axis of the cubic unit cell) widens

the band gap less than distortion along linear combinations of the B–X bond axes (e.g., 011 or 111). Given that we showed in the previous subsection that strain in different directions induces ferroelectric distortion along different crystallographic axes, this suggests the possibility that strain in different directions could lead to a wide range of band gaps.

In Group 14 (B = Ge, Sn, Pb) halide perovskites, the valence band is a combination of filled X-site p states and B-site s states, of which the VBM is the most antibonding combination. In the undistorted cubic structure, the VBM lies at k-point R = (1/2, 1/2, 1/2). The conduction band consists primarily of unfilled B-site p states. In the undistorted cubic structure, the CBM lies at k-point R = (1/2, 1/2, 1/2) and consists of threefold degenerate nonbonding combinations of B-site p states (p_x , p_y , and p_z). The near-gap band structure and computed electron densities of the band-edge crystal orbitals of cubic CsGeI₃ are shown in Figure 4b.

Most previous work aiming to understand the effects of distortion and strain on the electronic structure of halide perovskites has (for technological reasons) focused on Pb-based compounds, whose structural distortions take the form of octahedral rotations. ^{66–70} It stands to reason that the direction of strain in Ge-based compounds (and the associated variability in the direction of ferroelectric distortion) will also have a particularly strong effect on the band gaps and bandedge orbitals. This will be explored in the next subsection.

Effect of Strain on the Band Gap. When perovskite compounds undergo compressive and tensile biaxial strain in various crystallographic directions, their DFT-computed band gaps spread out to ranges of values. These ranges of band gaps are shown pictorially and numerically for DFT-HSE06 calculations in Figures 5 (for BaTiO₃) and 6 (for CsGeX₃).

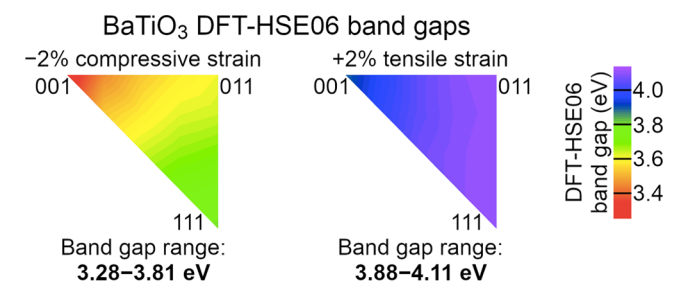


Figure 5. Heat maps of the DFT-HSE06-computed band gaps of biaxially strained $BaTiO_3$ strained perpendicular to various crystallographic axes (as in Figure 1c). The panel on the left shows -2% (compressive) strain, and the panel on the right shows +2% (tensile) strain. The numerical ranges of DFT-HSE06 band gaps are shown below each panel.

The numerical DFT-HSE06 results corresponding to Figures 5 and 6, as well as the corresponding DFT-PBE results that show similar trends, are provided in the Supporting Information.

We begin by focusing on the left side of Figure 5, BaTiO₃ under -2% compressive strain, to illustrate how these results can be interpreted. Among the directions of strain, the smallest band gap corresponds to strain perpendicular to the 001 axis (and consequent ferroelectric distortion in the 001 direction). The largest band gap corresponds to strain perpendicular to the 111 axis (and consequent ferroelectric distortion in the 111 direction). The band gaps in the left side of Figure 5 span the range 3.28-3.81 eV. The calculations show that changes in band gaps are brought about by shifts in the absolute energies

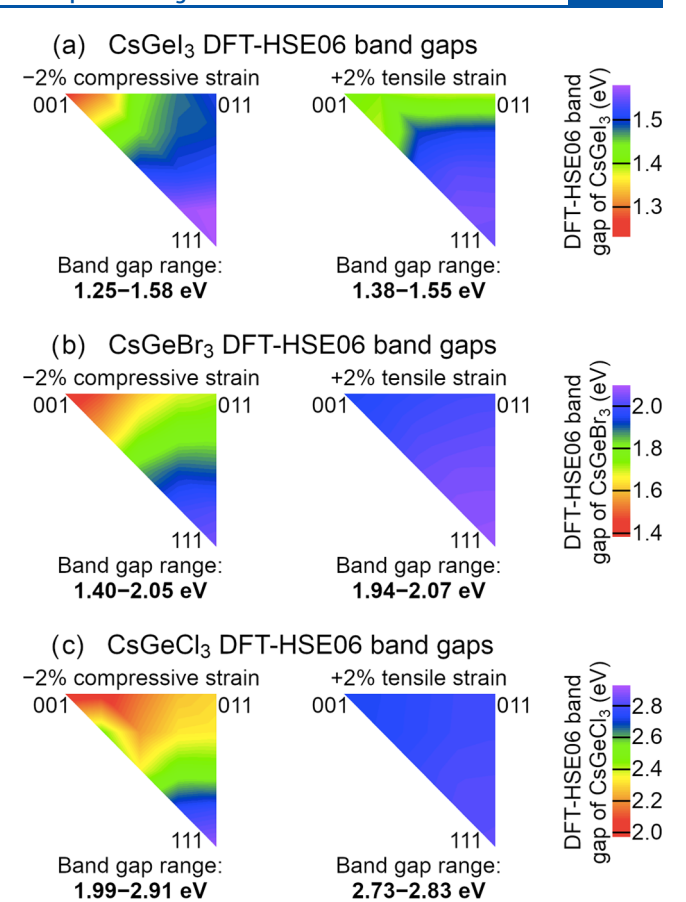


Figure 6. Heat maps of the DFT-HSE06-computed band gaps of biaxially strained (a) $CsGeI_3$, (b) $CsGeBr_3$, and (c) $CsGeCl_3$ strained perpendicular to various crystallographic axes (as shown in Figure 1c). Panels on the left show -2% (compressive) strain, and panels on the right show +2% (tensile) strain. The numerical ranges of DFT-HSE06 band gaps are shown below each panel.

of both band edges rather than just one (see Supporting Information); that is, a strain direction with a larger band gap has both a lower-energy VBM and a higher-energy CBM.

These qualitative findings are consistent with previous work on d^0 perovskite distortions, ⁶⁵ which explains based on the mixing of atomic orbitals at the band edges that ferroelectric distortion tends to widen band gaps more when oriented along a linear combination of the B–X bond axes. In the absence of distortion, the VBM of BaTiO₃ consists of oxide 2p states, while the CBM consists of titanium 3d states. Distortion lowers the structural symmetry, allowing oxide 2p and titanium 3d to mix in both band edges, pushing their energies apart. When distortion occurs along a Ti–O band axis (e.g., 001), this mixing occurs in only one or two of the threefold degenerate states at each band edge, which has little effect on the band gap. When distortion occurs along a linear combination of perovskite bond axes (e.g., 111), mixing occurs in all band-edge states, significantly widening the band gap.

From the standpoint of solar energy conversion, the ability to tune the band gap of $BaTiO_3$ (which has a large gap relative to the solar spectrum) has modest technological appeal, given the past interest in doped $BaTiO_3$. More generally, this is a clear demonstration that the direction of strain can significantly tune the band gap of a perovskite by tuning the direction of ferroelectric distortion.

Under +2% tensile strain (right side of Figure 5), BaTiO₃ band gaps are larger and somewhat less tunable. Computed gaps span the range 3.88–4.11 eV. The BaTiO₃ band gap is less sensitive to the direction of tensile strain than compressive strain because the various directions of tensile strain do not lead to as much variety in the crystallographic direction of ferroelectric distortion.

We next turn to CsGeX₃ germanium-halide perovskites, for which the effects of strain are similar to BaTiO₃ in some ways and different in others. Under -2% compressive strain in all directions (Figure 6a, left), DFT-HSE06 band gaps of CsGeI₃ range from 1.25-1.58 eV. This range is notable because it surrounds the optimal band gap for solar energy conversion according to Shockley and Queisser's analysis, 75 suggesting the possibility of efficient energy conversion in the most intense portion of the solar spectrum. Like BaTiO₃, the high end of the band gap range results from 111 strain and the low end from 001 strain. The band gap of CsGeI₃ under −2% 111 strain is similar to that of relaxed room-temperature CsGeI₃ (1.53 eV using DFT-HSE, 1.63 eV experimentally) because both have ferroelectric distortion along 111. Strains perpendicular to axes other than 111 reduce the band gap by redirecting the ferroelectric distortion along different crystallographic axes.

Under +2% tensile strain (Figure 6a, right), the band gap of CsGeI₃ remains in a similar range, though it does not vary as much with the direction of strain. DFT-HSE06 band gaps range from 1.38–1.55 eV. As was the case for BaTiO₃, the band gap of CsGeI₃ is less tunable under tensile strain because tensile strain does not direct ferroelectric distortion as reliably along the axis perpendicular to strain.

The analogous results for the other members of the germanium-halide series (X = Br, Cl) are shown in Figure 6b,c. Because the three germanium-halide compounds are isostructural and isoelectronic, some qualitative aspects of band gap tunability under biaxial strain are shared across the series. For all CsGeX3 compounds, band gaps are highly tunable via different directions of compressive strain, with the smallest band gaps occurring near the 001 strain direction and the largest occurring near the 111 strain direction. Furthermore, band gaps are significantly less tunable via different directions of tensile strain. There are differences among the germanium-halide compounds as well. Most significantly, band gaps increase (and become more tunable) with increasing electronegativity of the X-site anion as the valence band edge moves to lower energy. While this generally means the band gap of CsGeI3 lies closest to the optimal range for solar energy conversion, compressive strain of the other germanium-halides can bring their band gaps closer to the optimal range as well. Notably, the computed DFT-HSE06 band gap of CsGeBr3 can be reduced from 2.01 to 1.40 eV under -2% compressive strain in the 001 direction.

One remaining question is why, from an orbital standpoint, the band gaps of germanium-halide perovskites are so tunable with the varying direction of compressive strain, and, specifically, why their gaps are largest under 111 strain and smallest under 001 strain. Both DFT-PBE and DFT-HSE06 calculations show that the direction of strain and the consequent direction of ferroelectric distortion have a greater impact on the absolute energy of the VBM than that of the CBM (see Supporting Information). This makes qualitative sense, as the VBM is an antibonding combination of atomic orbitals that is therefore highly sensitive to changes in nearest-

neighbor interactions, while the CBM consists of nonbonding Ge 4p orbitals that are less sensitive to such changes.

The cause of the shift in VBM energy (and therefore band gap) with changing direction of strain and distortion is rationalized in Figure 7. Images in Figure 7 show the VBM of

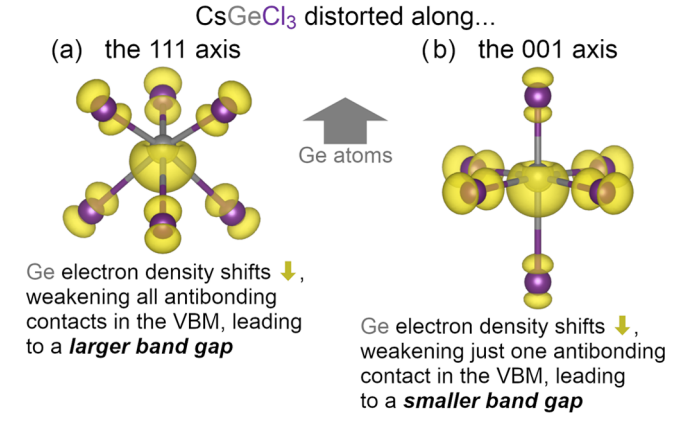


Figure 7. Electron densities associated with the DFT-PBE-computed valence band maxima (VBM) of $CsGeCl_3$ with ferroelectric distortion along the (a) 111 and (b) 001 axes. In both cases, the electron density surrounding the germanium cation shifts away from the nearestneighboring chlorine anions, weakening the antibonding interactions within the VBM. The distinction is that in panel (b), strong antibonding interactions remain at the equatorial positions, placing the VBM of the 001-distorted structure at a higher energy and giving it a smaller band gap.

CsGeCl₃ with ferroelectric distortion oriented along the 111 (Figure 7a) and 001 (Figure 7b) axes. The chloride compound is chosen because the movements of the electron density of its VBM are more visually pronounced than in the iodide or bromide compounds. (This is likely connected to the fact that the chloride compound shows the largest range of computed band gaps with changing direction of strain.) Both panels of the figure show a single distorted GeCl₆ octahedron oriented such that the germanium cation is shifted above the center of the octahedron. In both cases, to avoid close antibonding contacts with its nearest-neighboring chloride anions, the electron density surrounding germanium in the VBM shifts downward. In Figure 7a, this weakens all three of the strongest antibonding interactions, lowering the energy of the VBM and widening the band gap. In Figure 7b, the shift in electron density is only able to weaken one of the strongest antibonding interactions, leaving four around the equator, resulting in a higher-energy VBM and a narrower band gap. Therefore, because compressive strain perpendicular to 111 leads to distortion along 111, and compressive strain perpendicular to 001 leads to distortion closer to 001, compressive strain of germanium-halide perovskites perpendicular to 111 leads to the largest band gaps.

The Possibility of Tuning Band Gaps in Compounds with Octahedral Rotations. For the compounds discussed up to this point (BaTiO₃ and CsGeX₃), tunable ferroelectric distortions lead to wide band gap ranges, with changing direction of biaxial strain. However, in the field of perovskite photovoltaics, it is the lead-halide compounds—which feature primarily B—X octahedral rotations at room temperature—that have generated the most technological interest. In this subsection, we therefore consider the possibility that lead-halide perovskites may also be tuned via biaxial strain in all

directions. Our calculations focus on the room-temperature orthorhombic phase of CsPbI₃ under -2% compressive strain in all directions. In these calculations, the range of DFT-PBE band gaps is 1.81-1.84 eV, with no significant movement of either band edge (see Supporting Information for more details), suggesting that CsPbI₃ is less tunable than the polar compounds previously discussed. This is consistent with past computational results showing that the band gaps of the roomtemperature phases of lead- and tin-halide perovskites are relatively unaffected by the magnitude of biaxial strain.⁶⁹ However, given the shallow, complex potential energy landscapes of perovskites with octahedral rotations, it remains possible that strain in a variety of crystallographic directions could lead to phase transitions that significantly tune their band gaps. For example, CsPbI3 has been predicted to adopt a polar phase under tensile strain.⁷⁶ While full consideration of all possible phases under all directions of biaxial strain is beyond the scope of this paper, the existence of such phase transitions suggests possible routes toward greater tunability of lead-halide perovskite band gaps.

CONCLUSIONS

The results in this paper highlight and rationalize the extent to which the band gaps of oxide and halide perovskite compounds can be tuned by varying the magnitude and direction of biaxial strain. On the fundamental side, these findings illustrate how structural symmetry and interactions of atomic orbitals conspire to substantially raise and lower the energies of band-edge orbitals, consequently affecting a material's solar absorption behavior. On the applied side, these results suggest that if crystallites or local regions within a perovskite sample are nonuniformly strained in a variety of directions, a sample may have the ability to more efficiently absorb and convert light throughout the solar spectrum, akin to a multijunction solar cell. In particular, the germanium-halide perovskite results (e.g., CsGeI₃) suggest that compressive biaxial strain can bring band gaps into the optimal range for solar energy conversion.

ASSOCIATED CONTENT

Supporting Information

The Supporting Information is available free of charge at https://pubs.acs.org/doi/10.1021/acs.jpcc.1c07169.

Information about DFT pseudopotentials and tabulated numerical results corresponding to figures in the body of the paper can be found in the Supporting Information (PDF)

AUTHOR INFORMATION

Corresponding Author

Robert F. Berger – Department of Chemistry, Western Washington University, Bellingham 98225-9150 Washington, United States; orcid.org/0000-0002-2691-8667; Phone: (360) 650-4327; Email: bergerr@wwu.edu

Authors

Corey Teply – Department of Chemistry, Western Washington University, Bellingham 98225-9150 Washington, United States

Britt A. Tyler – Department of Chemistry, Western Washington University, Bellingham 98225-9150 Washington, United States

Complete contact information is available at:

https://pubs.acs.org/10.1021/acs.jpcc.1c07169

Notes

The authors declare no competing financial interest.

ACKNOWLEDGMENTS

pubs.acs.org/JPCC

This work is supported by the National Science Foundation under Award Number 2026970 and by the Research Corporation for Science Advancement through a Cottrell Scholar Award.

REFERENCES

- (1) Wrighton, M. S.; Ellis, A. B.; Wolczanski, P. T.; Morse, D. L.; Abrahamson, H. B.; Ginley, D. S. Strontium titanate photoelectrodes. Efficient photoassisted electrolysis of water at zero applied potential. *J. Am. Chem. Soc.* **1976**, *98*, 2774–2779.
- (2) Mavroides, J. G.; Kafalas, J. A.; Kolesar, D. F. Photoelectrolysis of water in cells with $SrTiO_3$ anodes. *Appl. Phys. Lett.* **1976**, 28, 241–243.
- (3) Kudo, A.; Miseki, Y. Heterogeneous photocatalyst materials for water splitting. *Chem. Soc. Rev.* **2009**, *38*, 253–278.
- (4) Kanhere, P.; Chen, Z. A review on visible light active perovskite-based photocatalysts. *Molecules* **2014**, *19*, 19995–20022.
- (5) Yin, W.-J.; Weng, B.; Ge, J.; Sun, Q.; Li, Z.; Yan, Y. Oxide perovskites, double perovskites and derivatives for electrocatalysis, photocatalysis, and photovoltaics. *Energy Environ. Sci.* **2019**, *12*, 442–462.
- (6) Kojima, A.; Teshima, K.; Shirai, Y.; Miyasaka, T. Organometal halide perovskites as visible-light sensitizers for photovoltaic cells. *J. Am. Chem. Soc.* **2009**, *131*, 6050–6051.
- (7) Park, N.-G. Perovskite solar cells: An emerging photovoltaic technology. *Mater. Today* **2015**, *18*, 65–72.
- (8) Snaith, H. J. Present status and future prospects of perovskite photovoltaics. *Nat. Mater.* **2018**, *17*, 372–376.
- (9) Jena, A. K.; Kulkarni, A.; Miyasaka, T. Halide perovskite photovoltaics: Background, status, and future prospects. *Chem. Rev.* **2019**, *119*, 3036–3103.
- (10) Kato, H.; Kudo, A. Visible-light-response and photocatalytic activities of TiO₂ and SrTiO₃ photocatalysts codoped with antimony and chromium. *J. Phys. Chem. B* **2002**, *106*, 5029–5034.
- (11) Konta, R.; Ishii, T.; Kato, H.; Kudo, A. Photocatalytic activities of noble metal ion doped SrTiO₃ under visible light irradiation. *J. Phys. Chem. B* **2004**, *108*, 8992–8995.
- (12) Iwashina, K.; Kudo, A. Rh-doped SrTiO₃ photocatalyst electrode showing cathodic photocurrent for water splitting under visible-light irradiation. *J. Am. Chem. Soc.* **2011**, *133*, 13272–13275.
- (13) Stoumpos, C. C.; Malliakas, C. D.; Kanatzidis, M. G. Semiconducting tin and lead iodide perovskites with organic cations: Phase transitions, high mobilities, and near-infrared photoluminescent properties. *Inorg. Chem.* **2013**, *52*, 9019–9038.
- (14) Noh, J. H.; Im, S. H.; Heo, J. H.; Mandal, T. N.; Seok, S. I. Chemical management for colorful, efficient, and stable inorganic-organic hybrid nanostructured solar cells. *Nano Lett.* **2013**, *13*, 1764–1769.
- (15) Hao, F.; Stoumpos, C. C.; Cao, D. H.; Chang, R. P. H.; Kanatzidis, M. G. Lead-free solid-state organic-inorganic halide perovskite solar cells. *Nat. Photonics* **2014**, *8*, 489–494.
- (16) McMeekin, D. P.; Sadoughi, G.; Rehman, W.; Eperon, G. E.; Saliba, M.; Hörantner, M. T.; Haghighirad, A.; Sakai, N.; Korte, L.; Rech, B.; et al. A mixed-cation lead mixed-halide perovskite absorber for tandem solar cells. *Science* **2016**, *351*, 151–155.
- (17) Slavney, A. H.; Hu, T.; Lindenberg, A. M.; Karunadasa, H. I. A bismuth-halide double perovskite with long carrier recombination lifetime for photovoltaic applications. *J. Am. Chem. Soc.* **2016**, *138*, 2138–2141.
- (18) Etgar, L.; Gao, P.; Xue, Z.; Peng, Q.; Chandiran, A. K.; Liu, B.; Nazeeruddin, M. K.; Grätzel, M. Mesoscopic CH₃NH₃PbI₃/TiO₂ heterojunction solar cells. *J. Am. Chem. Soc.* **2012**, *134*, 17396–17399.

- (19) Laban, W. A.; Etgar, L. Depleted hole conductor-free lead halide iodide heterojunction solar cells. *Energy Environ. Sci.* **2013**, *6*, 3249–3253.
- (20) You, J.; Hong, Z.; Yang, Y.; Chen, Q.; Cai, M.; Song, T.-B.; Chen, C.-C.; Lu, S.; Liu, Y.; Zhou, H.; et al. Low-temperature solution-processed perovskite solar cells with high efficiency and flexibility. ACS Nano 2014, 8, 1674–1680.
- (21) Tan, H.; Zhao, Z.; Zhu, W.-B.; Coker, E. N.; Li, B.; Zheng, M.; You, W.; Fan, H.; Sun, Z. Oxygen vacancy enhanced photocatalytic activity of perovskite SrTiO₃. ACS Appl. Mater. Interfaces **2014**, 6, 19184–19190.
- (22) Mitzi, D. B.; Feild, C. A.; Harrison, W. T. A.; Guloy, A. M. Conducting tin halides with a layered organic-based perovskite structure. *Nature* **1994**, *369*, 467–469.
- (23) Mitzi, D. B.; Wang, S.; Feild, C. A.; Chess, C. A.; Guloy, A. M. Conducting layered organic-inorganic halides containing (110)-oriented perovskite sheets. *Science* **1995**, *267*, 1473–1476.
- (24) Lee, C.-H.; Podraza, N. J.; Zhu, Y.; Berger, R. F.; Shen, S.; Sestak, M.; Collins, R. W.; Kourkoutis, L. F.; Mundy, J. A.; Wang, H.; et al. Effect of reduced dimensionality on the optical band gap of SrTiO₃. *Appl. Phys. Lett.* **2013**, *102*, No. 122901.
- (25) Stoumpos, C. C.; Cao, D. H.; Clark, D. J.; Young, J.; Rondinelli, J. M.; Jang, J. I.; Hupp, J. T.; Kanatzidis, M. G. Ruddlesden-Popper hybrid lead iodide perovskite 2D homologous semiconductors. *Chem. Mater.* **2016**, 28, 2852–2867.
- (26) Tsai, H.; Nie, W.; Blancon, J. C.; Stoumpos, C. C.; Asadpour, R.; Harutyunyan, B.; Neukirch, A. J.; Verduzco, R.; Crochet, J. J.; Tretiak, S.; et al. High-efficiency two-dimensional Ruddlesden-Popper perovskite solar cells. *Nature* **2016**, *536*, 312–316.
- (27) Schlom, D. G.; Chen, L.-Q.; Eom, C.-B.; Rabe, K. M.; Streiffer, S. K.; Triscone, J.-M. Strain tuning of ferroelectric thin films. *Annu. Rev. Mater. Res.* **2007**, *37*, 589–626.
- (28) Schlom, D. G.; Chen, L.-Q.; Fennie, C. J.; Gopalan, V.; Muller, D. A.; Pan, X.; Ramesh, R.; Uecker, R. Elastic strain engineering of ferric oxides. MRS Bull. 2014, 39, 118–130.
- (29) Hwang, J.; Feng, Z.; Charles, N.; Wang, X. R.; Lee, D.; Stoerzinger, K. A.; Muy, S.; Rao, R. R.; Lee, D.; Jacobs, R.; et al. Tuning perovskite oxides by strain: Electronic structure, properties, and functions in (electro)catalysis and ferroelectricity. *Mater. Today* **2019**, *31*, 100–118.
- (30) Wang, Y.; Sun, X.; Chen, Z.; Sun, Y.-Y.; Zhang, S.; Lu, T.-M.; Wertz, E.; Shi, J. High-temperature ionic epitaxy of halide perovskite thin film and the hidden carrier dynamics. *Adv. Mater.* **2017**, 29, No. 1702643.
- (31) Wang, L.; Chen, P.; Thongprong, N.; Young, M.; Kuttipillai, P. S.; Jiang, C.; Zhang, P.; Sun, K.; Duxbury, P. M.; Lunt, R. R. Unlocking the single-domain epitaxy of halide perovskites. *Adv. Mater. Interfaces* **2017**, *4*, No. 1701003.
- (32) Chen, J.; Morrow, D. J.; Fu, Y.; Zheng, W.; Zhao, Y.; Dang, L.; Stolt, M. J.; Kohler, D. D.; Wang, X.; Czech, K. J.; et al. Single-crystal thin films of cesium lead bromide perovskite epitaxially grown on metal oxide perovskite (SrTiO₃). *J. Am. Chem. Soc.* **2017**, *139*, 13525–13532.
- (33) Chen, Y.; Lei, Y.; Li, Y.; Yu, Y.; Cai, J.; Chiu, M.-H.; Rao, R.; Gu, Y.; Wang, C.; Choi, W.; et al. Strain engineering and epitaxial stabilization of halide perovskites. *Nature* **2020**, *577*, 209–215.
- (34) Huang, H. Ferroelectric photovoltaics. *Nat. Photonics* **2010**, *4*, 134–135.
- (35) Butler, K. T.; Frost, J. M.; Walsh, A. Ferroelectric materials for solar energy conversion: Photoferroics revisited. *Energy Environ. Sci.* **2015**, *8*, 838–848.
- (36) Chen, B.; Shi, J.; Zheng, X.; Zhou, Y.; Zhu, K.; Priya, S. Ferroelectric solar cells based on inorganic-organic hybrid perovskites. *J. Mater. Chem. A* **2015**, *3*, 7699–7705.
- (37) Krishnamoorthy, T.; Ding, H.; Yan, C.; Leong, W. L.; Baikie, T.; Zhang, Z.; Sherburne, M.; Li, S.; Asta, M.; Mathews, N.; et al. Lead-free germanium iodide perovskite materials for photovoltaic applications. *J. Mater. Chem. A* **2015**, *3*, 23829–23832.

- (38) Stoumpos, C. C.; Frazer, L.; Clark, D. J.; Kim, Y. S.; Rhim, S. H.; Freeman, A. J.; Ketterson, J. B.; Kang, J. I.; Kanatzidis, M. G. Hybrid germanium iodide perovskite semiconductors: Active lone pairs, structural distortions, direct and indirect energy gaps, and strong nonlinear optical properties. *J. Am. Chem. Soc.* **2015**, *137*, 6804–6819.
- (39) Ming, W.; Shi, H.; Du, M.-H. Large dielectric constant, high acceptor density, and deep electron traps in perovskite solar cell material CsGeI₃. *J. Mater. Chem. A* **2016**, *4*, 13852–13858.
- (40) Liu, D.; Li, Q.; Jing, H.; Wu, K. Pressure-induced effects in the inorganic halide perovskite CsGeI₃. RSC Adv. **2019**, *9*, 3279–3284.
- (41) Kresse, G.; Hafner, J. Ab initio molecular dynamics for liquid metals. *Phys. Rev. B* **1993**, *47*, 558–561.
- (42) Kresse, G.; Hafner, J. Ab initio molecular-dynamics simulation of the liquid-metal—amorphous-semiconductor transition in germanium. *Phys. Rev. B* **1994**, *49*, 14251–14269.
- (43) Kresse, G.; Furthmüller, J. Efficiency of ab-initio total energy calculations for metals and semiconductors using a plane-wave bases set. *Comput. Mater. Sci.* **1996**, *6*, 15–50.
- (44) Kresse, G.; Furthmüller, J. Efficient iterative schemes for ab initio total-energy calculations using a plane-wave basis set. *Phys. Rev.* B 1996, 54, 11169–11186.
- (45) Kresse, G.; Joubert, D. From ultrasoft pseudopotentials to the projector augmented-wave method. *Phys. Rev. B* **1999**, *59*, 1758–1775.
- (46) See Supporting Information at [URL will be inserted by publisher] for pseudopotential details and tables with numerical results corresponding to figures in the body of the paper.
- (47) Perdew, J. P.; Burke, K.; Ernzerhof, M. Generalized gradient approximation made simple. *Phys. Rev. Lett.* **1996**, *77*, 3865–3868.
- (48) Krukau, A. V.; Vydrov, O. A.; Izmaylov, A. F.; Scuseria, G. E. Influence of the exchange screening parameter on the performance of screened hybrid functionals. *J. Chem. Phys.* **2006**, 125, No. 224106.
- (49) Suzuki, K.; Kijima, K. Optical band gap of barium titanate nanoparticles prepared by RF-plasma chemical vapor deposition. *Jpn. J. Appl. Phys.* **2005**, *44*, 2081–2082.
- (50) Choi, K. J.; Biegalski, M.; Li, Y. L.; Sharan, A.; Schubert, J.; Uecker, R.; Reiche, P.; Chen, Y. B.; Pan, X. Q.; Gopalan, V.; et al. Enhancement of ferroelectricity in strained BaTiO₃ thin films. *Science* **2004**, *306*, 1005–1009.
- (51) Pertsev, N. A.; Zembilgotov, A. G.; Tagantsev, A. K. Effect of mechanical boundary conditions on phase diagrams of epitaxial ferroelectric thin films. *Phys. Rev. Lett.* **1998**, *80*, 1988–1991.
- (52) Goldschmidt, V. M. Die Gesetze der Krystallochemie. Naturwissenschaften 1926, 14, 477.
- (53) Bartel, C. J.; Sutton, C.; Goldsmith, B. R.; Ouyang, R.; Musgrave, C. B.; Ghiringhelli, L. M.; Scheffler, M. New tolerance factor to predict the stability of perovskite oxides and halides. *Sci. Adv.* **2019**, *5*, No. eaav0693.
- (54) Shannon, R. D. Revised effective ionic radii and systematic studies of interatomic distances in halides and chalcogenides. *Acta Cryst. A* **1976**, 32, 751–767.
- (55) Smith, M. B.; Page, K.; Siegrist, T.; Redmond, P. L.; Walter, E. C.; Seshadri, R.; Brus, L. E.; Steigerwald, M. L. Crystal structure and the paraelectric-to-ferroelectric phase transition of nanoscale BaTiO₃. *J. Am. Chem. Soc.* **2008**, *130*, 6955–6963.
- (56) Thiele, G.; Rotter, H. W.; Schmidt, K. D. Kristallstrukturen und Phasentransformationen von Caesiumtrihalogenogermanaten(II) CsGeX₃ (X = Cl, Br, I). *Z. Anorg. Allg. Chem.* **1987**, *545*, 148–156.
- (57) Momma, K.; Izumi, F. VESTA 3 for three-dimensional visualization of crystal, volumetric and morphology data. *J. Appl. Crystallogr.* **2011**, *44*, 1272–1276.
- (58) Piskunov, S.; Heifets, E.; Eglitis, R. I.; Borstel, G. Bulk properties and electronic structure of SrTiO₃, BaTiO₃, PbTiO₃ perovskites: An ab initio HF/DFT study. *Comput. Mater. Sci.* **2004**, 29, 165–178.
- (59) Berger, R. F.; Fennie, C. J.; Neaton, J. B. Band gap and edge engineering via ferroic distortion and anisotropic strain: The case of SrTiO₃. *Phys. Rev. Lett.* **2011**, *107*, No. 146804.

- (60) Brivio, F.; Walker, A. B.; Walsh, A. Structural and electronic properties of hybrid perovskites for high-efficiency thin-film photovoltaics from first-principles. *APL Mater.* **2013**, *1*, No. 042111.
- (61) Brivio, F.; Butler, K. T.; Walsh, A.; van Schilfgaarde, M. Relativistic quasiparticle self-consistent electronic structure of hybrid halide perovskite photovoltaic absorbers. *Phys. Rev. B* **2014**, *89*, No. 155204.
- (62) Yin, W.-J.; Yang, J.-H.; Kang, J.; Yan, Y.; Wei, S.-H. Halide perovskite materials for solar cells: A theoretical review. *J. Mater. Chem. A* **2015**, *3*, 8926–8942.
- (63) Berger, R. F. Design principles for the atomic and electronic structure of halide perovskite photovoltaic materials: Insights from computation. *Chem.–Eur. J.* **2018**, *24*, 8708–8716.
- (64) Goesten, M. G.; Hoffmann, R. Mirrors of bonding in metal halide perovskites. J. Am. Chem. Soc. 2018, 140, 12996–13010.
- (65) Ĉirlincione, D. V.; Berger, R. F. Tuning the electronic structure of d^0 perovskite oxides by combining distortive modes. *Phys. Rev. B* **2021**, *103*, No. 045127.
- (66) Amat, A.; Mosconi, E.; Ronca, E.; Quarti, C.; Umari, P.; Nazeeruddin, M. K.; Grätzel, M.; Angelis, F. D. Cation-induced bandgap tuning in organohalide perovskites: Interplay of spin-orbit coupling and octahedra tilting. *Nano Lett.* **2014**, *14*, 3608–3616.
- (67) Filip, M. R.; Eperon, G. E.; Snaith, H. J.; Giustino, F. Steric engineering of metal-halide perovskites with tunable optical band gaps. *Nat. Commun.* **2014**, *5*, No. 5757.
- (68) Motta, C.; El-Mellouhi, F.; Kais, S.; Tabet, N.; Alharbi, F.; Sanvito, S. Revealing the role of organic cations in hybrid halide perovskite CH₃NH₃PbI₃. *Nat. Commun.* **2015**, *6*, No. 7026.
- (69) Grote, C.; Berger, R. F. Strain tuning of tin—halide and lead—halide perovskites: A first-principles atomic and electronic structure study. *J. Phys. Chem. C* **2015**, *119*, 22832—22837.
- (70) Wang, T.; Daiber, B.; Frost, J. M.; Mann, S. A.; Garnett, E. C.; Walsh, A.; Ehrler, B. Indirect to direct bandgap transition in methylammonium lead halide perovskite. *Energy Environ. Sci.* **2017**, *10*, 509–515.
- (71) Upadhyay, S.; Shrivastava, J.; Solanki, A.; Choudhary, S.; Sharma, V.; Kumar, P.; Singh, N.; Satsangi, V. R.; Shrivastav, R.; Waghmare, U. V.; et al. Enhanced photoelectrochemical response of BaTiO₃ with Fe doping: Experiments and first-principles analysis. *J. Phys. Chem. C* **2011**, *115*, 24373–24380.
- (72) Cao, J.; Ji, Y.; Tian, C.; Yi, Z. Synthesis and enhancement of visible light activities of nitrogen-doped BaTiO₃. *J. Alloys Compd.* **2014**, *615*, 243–248.
- (73) Yang, F.; Lin, S.; Yang, L.; Liao, J.; Chen, Y.; Wang, C.-Z. First-principles investigation of metal-doped cubic BaTiO₃. *Mater. Res. Bull.* **2017**, *96*, 372–378.
- (74) Yang, F.; Yang, L.; Ai, C.; Xie, P.; Lin, S.; Wang, C.-Z.; Lu, X. Tailoring bandgap of perovskite BaTiO₃ by transition metals codoping for visible-light photoelectrical applications: A first-principles study. *Nanomaterials* **2018**, *8*, 455.
- (75) Shockley, W.; Queisser, H. J. Detailed balance limit of efficiency of p-n junction solar cells. *J. Appl. Phys.* **1961**, 32, 510–519.
- (76) Leppert, L.; Reyes-Lillo, S. E.; Neaton, J. B. Electric field- and strain-induced Rashba effect in hybrid halide perovskites. *J. Phys. Chem. Lett.* **2016**, *7*, 3683–3689.